An Unassisted Super-Resolution Satellite Navigation Receiver Using GPS L5 Signals

Yiran Luo, Li-Ta Hsu, *Member, IEEE*, Chin Lok Tsang, and Naser El-Sheimy

***Abstract*—Many existing works use external devices or information, e.g., real-world maps, reference receivers, dead reckoning (DR) sensors, and multi-antennas, to compensate for signal dynamics and mitigate multipath interference in global navigation satellite system (GNSS) signal reception. This paper proposes a standalone GPS L5 receiver using the fractional Fourier transform (FRFT) in an over-one-second super-long coherent integration (S-LCI) correlating process. Then, a code phase DR method is presented in the baseband processing by leveraging the super-resolution (SR) average Doppler rate and instantaneous Doppler frequency from the S-LCI-based FRFT to enhance the code discriminating process. A software-defined radio (SDR) prototype of the unassisted super-resolution receiver (U-SRR) based on the S-LCI, FRFT, and code phase DR is developed where the pilot-channel L5 signal serves for positioning. The transmitting time splicing comes from the respective frame synchronization and code phase tracking in the data and pilot channels. Real-world experiments verify the proposed U-SRR in an extremely dense-urban area. Compared to the legacy L1 C/A signals from the u-blox F9P receiver, the code-based positioning precision is increased by 86.8% with 100% measurement availability.**

***Index Terms*—GPS L5 pilot channel, code phase dead reckoning (DR), super-resolution signal processing, super-long coherent integration (S-LCI), fractional Fourier transform (FRFT), cross-ambiguity function (CAF), multipath mitigation**

I. Introduction

HIGH-PRECISION positioning using Global Navigation Satellite System (GNSS) receivers in urban areas is of utmost importance. The GNSS receiver has an unparalleled capability of providing users with accurate global absolute positioning solutions. However, The baseband of GNSS receivers faces significant challenges when operating in urban environments, which can result in interruptions to the continuity and quality of the measurements obtained. That means the GNSS positioning results will be intimately affected. For example, the severe multipath and non-line-of-sight (NLOS) interference, as well as a signal interruption and power attenuation, can significantly impede the ability of the baseband processing of GNSS receivers to estimate line-of-sight (LOS) signals [1]–[3].

Multipath signals can distort correlation gain distribution varying with code offset, impacting GNSS positioning accuracy. The prior art utilizing multi-correlators resisting multipath interference in code phase estimation can perform without external devices or information [4]–[6]. Despite their overall effectiveness, current methods have limitations in improving the navigation performance of GNSS receivers in urban environments. To further enhance the navigation capabilities of GNSS receivers, numerous approaches have been developed that utilize additional data sources beyond the receiver itself.

The vision correlator elevates a conventional multipath mitigation technique (MMT) [7], and it has been verified with live data in a multipath environment [8]. However this technique necessitates the formation of a reference function shape derived from either a long-term real-world experiment or a high-quality simulator. Besides, multi-antenna arrays offer strong multipath mitigation capabilities in difficult environments but at the cost of increased hardware expenses [9]–[11]. Moreover, artificial intelligence is also being used to categorize GNSS baseband output features into LOS/Multipath/NLOS signals, thereby enhancing positioning accuracy in urban areas. [12]. However, This approach demands using a simulator to generate GNSS signals, followed by integrating real-world maps and three-dimension (3D) building models for labeling and training purpose.

Another work that models the NLOS path of the baseband signal, i.e., the cross-ambiguity function (CAF) [13], uses the Google Map [14], [15]. This research explores the super-long coherent integration (S-LCI) for separating the multipath signals with an ultra-stable oscillator with the aid of Doppler rate estimation from a reference receiver. Furthermore, the ultra-tightly coupling technique, where the inertial sensor deeply aids the GNSS baseband, is also prevalently discussed to achieve high sensitivity in urban and indoor navigation [16]. It is apparent that the techniques above require supplementary external devices and information.

In a multipath channel with both LOS and NLOS signals, long coherent integration, offering higher frequency resolution than short coherent integration, better separates the desired signal (i.e., the LOS signal) from the interference (i.e., the NLOS signals) [15]. Besides, low-cost GNSS devices with a one-second S-LCI implementation have also demonstrated accurate positioning performance in urban canyons [17], [18]. Nevertheless, some issues are occurring to the existing works as:

1) Most related research requires an aided-GNSS procedure or a maximum power estimator to exclude the bit transition that reduce the correlator output performance in an on-the-fly system [15], [19], [20];
2) Increasing the coherent integration time has the potential to improve the tracking performance for multipath mitigation, but present GNSS receivers applicable to the

Yiran Luo and Naser El-Sheimy are with the Department of Geomatics Engineering, University of Calgary, Calgary T2N1N4, Canada (e-mail: yiran.luo@ucalgary.ca; elsheimy@ucalgary.ca).

Li-Ta Hsu and Chin Lok Tsang are with the Department of Aeronautical and Aviation Engineering, The Hong Kong Polytechnic University, Hong Kong SAR, China (e-mail: lt.hsu@polyu.edu.hk; chin-lok.au.tsang@connect.polyu.hk).

real world are seldom based on an S-LCI interval over 1 second [2], [17], [18];
3) Existing S-LCI procedures in GNSS overly depend on the subspace of signal frequency, causing it too challenging to separate the LOS and NLOS signals, e.g., demanding an over-100-s integration time [14], [15];
4) How the baseband GNSS CAF formed with the S-LCI approach can suppress the random noise of the navigation results is not adequately discussed.
5) In the S-LCI implementation, the correlation power affected by higher-order dynamics (i.e., the Doppler rate) still needs investigating though accumulated phase error and code grid migration have been discussed in a recent research work [19].

We have covered parts of the research gaps in our previous research. For example, a previous reference proves that the Doppler rate intimately affects the CAF signal power in the highly extended coherent integration procedure [15]. In that case, we applied the fractional Fourier transform (FRFT) to the GNSS baseband such that the available subspaces in terms of the S-LCI CAF estimation are expanded as both signal frequency shift and rate domains instead of the frequency shift only [21]–[24]. However, some research work remains to be completed:

1) How the FRFT copes with random noise in positioning has not been addressed though we applied an absolute-position-aided (APA) method in GNSS code tracking to reduce the biased error in positioning [25], [26].
2) How a coherent integration technique with FRFT using more than one second time can surpass the one-second coherent integration in GNSS positioning needs to excavate;
3) The present works demonstrated that the FRFT could enhance the GNSS signal acquisition [22], tracking [27], and extracted measurements [24] when the Doppler rate exists. However, the GNSS positioning performance with the FRFT-based processing is seldom evaluated;
4) Detailed theoretical analysis of the GNSS baseband processing based on the FRFT was provided [23], [24]. Still, there is a lack of practical experiments in a challenging environment to show its feasibility in the real world.

Modernized GPS L5 signals are transmitted in both data and pilot channels which synchronize with the oscillator [28]. The pilot channel includes no navigation data, so it is available for a long correlating process without external aiding. This research is an upgraded version of our previous works based on these introductions. We propose a super-resolution (SR) satellite navigation receiver using GPS L5 signals. The navigation system is standalone and unassisted with external hardware devices or data sources such as inertial sensors, reference receivers, real-world maps, pre-processing experiments, or multi-antennas. Then, the main contributions of this paper are summarized as follows:

1) A code phase dead reckoning (DR) approach regarding the GNSS baseband processing is proposed leveraging the SR average Doppler rate and instantaneous Doppler frequency, resisting the code delay error caused by traditional code discriminators in a severe multipath/NLOS environment;
2) An unassisted tracking architecture for GPS L5 signals based on the over-one-second S-LCI technique is proposed on a software-defined radio (SDR) receiver;
3) The FRFT is integrated into the S-LCI GNSS baseband processing, and we evaluate not only the baseband outputs (correlations, code phase, and Doppler frequency errors) but also the positioning results;
4) The intermediate frequency (IF) GPS L5 signals collected in a real-world dense-urban area in Hong Kong are processed with the proposed SDR prototype to verify its application feasibility and prospect in the commercial market.

Finally, we compare the proposed and conventional GNSS receivers in terms of the code signal baseband processing in Table I where FRFD and NCO correspond to fractional Fourier domain and numerically controlled oscillator, respectively, and new signal processing algorithms proposed in this work are highlighted with bold fonts.

TABLE I
COMPARISON OF THE OLD AND PROPOSED GNSS CODE SIGNAL BASEBAND PROCESSING.

Baseband Processing Block	Old [29]	Proposed
Correlator	Old Fourier/ frequency domain	FRFD
Coherent integration	$\leq 20ms$	$\geq 1s$ (1s, 5s, and 10s were tested)
Code phase discriminator	Early-late envelope/ power, etc.	**Not used**
Code loop filter	2nd-order	**Not used (open loop)**
Code NCO frequency computation	Average	**Instantaneous (via DR)**
Pseudorange computation	Instantaneous (via NCO with absolute code phase update)	**Instantaneous (via NCO without absolute code phase update/ with pure DR)**

The paper is organized as follows. Section II explores the generic architecture of the proposed unassisted SR receiver (U-SRR); Section III elaborates on the system design algorithms for the baseband signal processing, measurements extraction, and navigation algorithms; how to compute the Doppler and time-of-arrival (TOA) references is included in Section IV; the approach to remove the initial code phase error is provided in Section V; Section VI describes the real-world experiments and discusses the results; finally, Section VII concludes this paper.

II. ARCHITECTURE OF THE UNASSISTED SUPER-RESOLUTION RECEIVER USING L5 SIGNALS

Fig. 1 illustrates the proposed SDR work process diagram without external assistance. In this system, an acquisition algorithm based on the 100-ms parallel code search (PCS) is implemented on the pilot-channel L5 signal, i.e., L5Q, to obtain the initial Doppler frequency and code phase once the incoming L5 signals are transferred to the IF through a GNSS frontend [30]. Then, these initial guesses are conveyed

to the tracking block to initialize the proposed baseband signal processing algorithm.

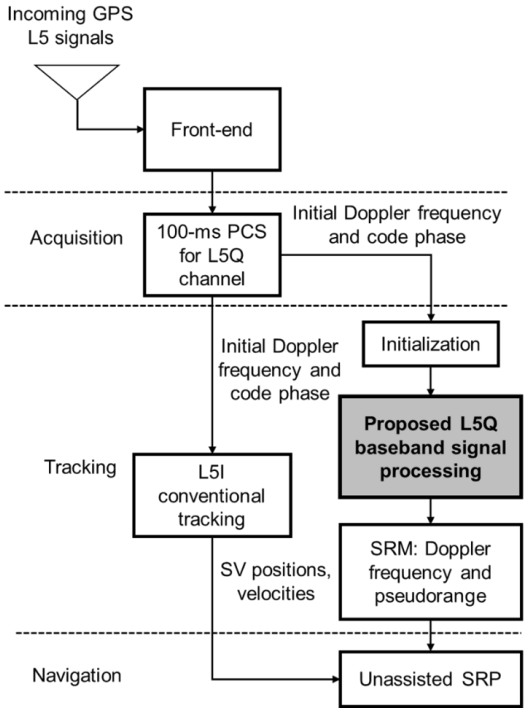

Fig. 1. Diagram of the proposed GNSS U-SRR using GPS L5 signals.

As shown in Fig. 2, the initialization adopts the conventional tracking (CT) algorithms to estimate the code and carrier phases in the SDR [31]. Then, the SDR synchronizes the bits of the Neuman- Hoffman (NH) sequence based on a histogram approach [32]. The baseband activates the proposed SR signal processing after the initialization. Then, it produces super-resolution measurements (SRMs), i.e., Doppler frequencies and pseudoranges.

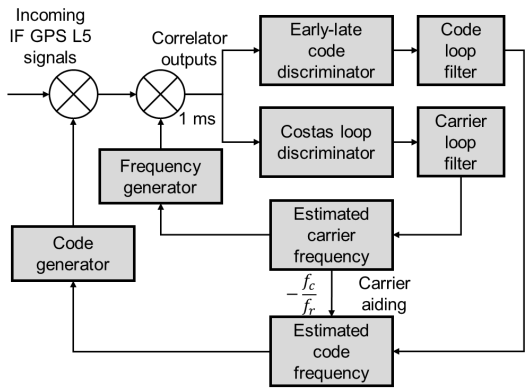

Fig. 2. Architecture of the conventional tracking process.

It is worth mentioning that the pilot channel of L5 signals does not transmit the bit streams for navigation purposes, but the other data channel, i.e., L5I, does not have this limitation. Thus, the two types of L5 channels collaborate in this system where the data channel extracts the ephemeris from the data bits using the essential CT [32], [33], while the pilot counterpart offers the ranging measurements to achieve super-resolution positioning (SRP).

The baseband signal processing design plays another vital role in the proposed U-SRR, which involves the main contributions of this work. So, the proposed baseband processing using the L5Q signals is provided in Fig. 3, where the architecture upgrades the baseband processing from the following aspects:

First, the S-LCI interval (not less than 1 s) is used to form the baseband correlation;

Second, the S-LCI correlation is transferred to the fractional Fourier domain (FRFD) to compensate for the power loss caused by the Doppler-rate-induced carrier phase error such that an SR Doppler frequency can be estimated;

Last but not least, the traditional code discriminator (e.g., an early-late envelope/power discriminator) is omitted, and, instead, the estimated SR Doppler frequency takes full charge of the code numerically controlled oscillator (NCO) frequency estimation (i.e., a code phase DR method);

In summary, this section introduces the generic architecture of the proposed U-SRR system and will investigate detailed system design algorithms subsequently.

III. System design

A. Super-resolution baseband processing for the L5Q signal

The radio frequency (RF) GPS L5 signal from a single satellite is expressed as [28], [33]

$$\begin{aligned}&\tilde{r}_{IF}(t)\\&=\sqrt{P}c_{I5}(t-\tau)\,b_{I5}(t-\tau)\,D(t-\tau)\cos(\phi_{IF}(t))\\&\quad+\sqrt{P}c_{Q5}(t-\tau)\,b_{Q5}(t-\tau)\sin(\phi_{IF}(t))+n_{IF}(t)\end{aligned}\tag{1}$$

where $\tilde{r}_{IF}(t)$ is the incoming IF signal; P is the received signal power combined with the L5I and L5Q in Watts; $c_{I5}(t)$ and $c_{Q5}(t)$ are the waveforms of the spreading codes of L5I and L5Q, respectively; $D(t)$ is the waveform of the data bit stream for L5I while the L5Q is free of data bit modulation; $b_{I5}(t)$ is the secondary code, i.e., the NH code, for the L5I, and it is deterministic and has 10 bits with a periodic 10-ms length; analogously, $b_{Q5}(t)$ is the periodic NH code waveform for the L5Q, and it has 20 bits within a 20-ms period; τ is the time delay over the signal transmission path from the satellite to the user's antenna; $\phi_{IF}(t)$ is the received IF carrier phase varied with the time variable; $n_{IF}(t)$ denotes the complex Gaussian white noise, and its power spectral density is N_0 W/Hz.

1) L5Q baseband signal model in the FRFD: Once the bits of the L5Q channel are synchronized, the NH sequence is determined for the local replicas. Then, the locally replicated signal of L5Q can be expressed as

$$\hat{r}_{IF,Q5}(t)=c_{Q5}(t-\hat{\tau})\,b_{Q5}(t-\hat{\tau})\,e^{j2\pi\left(f_I+\hat{f}\right)t+j\hat{\phi}}\tag{2}$$

where $\hat{\tau}$, $\hat{f}$, and $\hat{\phi}$ are the replicated code phase delay, Doppler frequency, and carrier phase, respectively. Then, dumping and integrating the incoming IF signal with (2) gives the discrete baseband signal model as [23]

$$\begin{aligned}\tilde{\chi}_{Q5}(\Delta\tau,\Delta f)[n_S]&=aR_{cc}(\Delta\tau)\,\mathrm{sinc}\left(\Delta fT_S+\tfrac{\mu}{2}n_ST_S^2\right)\\&\quad\times\exp\left(j\Delta\phi+j2\pi\Delta fn_ST_S+j\mu n_S^2T_S^2\right)+n_{Q5,n_S}\end{aligned}\tag{3}$$

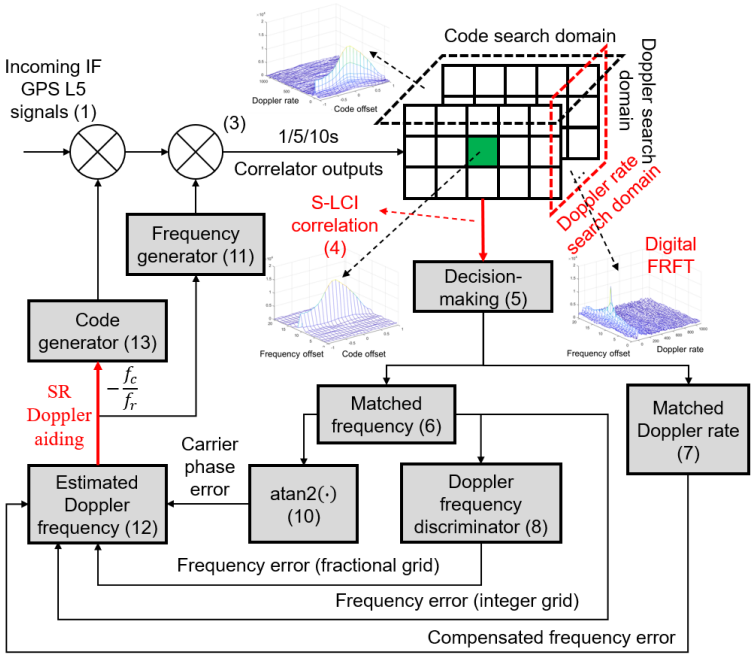

Fig. 3. Architecture of the proposed GPS L5Q baseband signal processing using the S-LCI, FRFT, and SR Doppler aiding algorithms. The main contributions corresponding to improving the GNSS baseband tracking technique are highlighted in red.

where $\Delta\tau = \tau - \hat{\tau}$, $\Delta f = f - \hat{f}$, $\Delta\phi = \phi - \hat{\phi}$; the subscript n_S denotes the index of coherent samples within a single S-LCI interval; $\Delta\tau$, Δf, $\Delta\phi$ are the code delay error, Doppler frequency error, and the carrier phase error, respectively; μ denotes the Doppler rate of the received signal; $R_{cc}(\cdot)$ is the cross-correlation function of the spreading codes; n_{Q5,n_S} represents the complex random noise for the baseband signals. a is the amplitude of the baseband signal $\sqrt{P}/2$. Regardless of noise, $\chi_{Q5}(\Delta\tau, \Delta f)[n_S]$ is the function relative to the code and frequency offsets; it is called the CAF and represents a discrete correlating sample in the slow-time domain.

Next, omitting the variable denotations $\Delta\tau$ and Δf in the CAF signal model, taking digital FRFT for (3) gives the model of the S-LCI correlation in the FRFD as (4) [34], [35] for $\frac{m_u}{2\sqrt{N_S}} = -\frac{M_u-1}{2}, \cdots, \frac{M_u-1}{2}$, $m_p = -\frac{M_p-1}{2}, \cdots, \frac{M_p-1}{2}$, $m_u, m_p \in \mathbb{Z}$, where m_u and m_p represent the indexes of the match filters for frequency shift and FRFT order (related to Doppler rate) in the FRFD, respectively; Δp is the discrete search step for the FRFT order; M_u, and M_p are the numbers of match filters in the FRFD (matching frequency shift and frequency rate, respectively); N_S is the number of $\chi_{Q5}(\Delta\tau, \Delta f)[n_S]$ over an S-LCI interval.

2) Estimation of the super-resolution Doppler frequency and Doppler rate: When the FRFT is applied to the original baseband CAF signals, it jointly forms a matching filter process for the unknown Doppler shift and rate. For

$$\begin{aligned}\mathcal{N}_{m_c} &= \{x | -1/d_c < x < 1/d_c, x \in \mathbb{Z}\}\\ \mathcal{N}_{m_u} &= \left\{x | -N_S\sqrt{N_S} < x < N_S\sqrt{N_S}, x \in \mathbb{Z}\right\}\\ \mathcal{N}_{m_p} &= \{x | -1/\Delta p < x < 1/\Delta p, x \in \mathbb{Z}\}\end{aligned}$$

where d_c is the spacing of two adjacent code match filters in chips, and Δp is the FRFT order step; then, the decision-making for these three parameters is expressed as

$$\left[\hat{m}_c, \hat{m}_u, \hat{m}_p\right] = \underset{\substack{m_c \in \mathcal{N}_{m_c}\\ m_u \in \mathcal{N}_{m_u}\\ m_p \in \mathcal{N}_{m_p}}}{\operatorname{argmax}} \left\{\left|DF^p\left\{\tilde{\chi}_{Q5}\left[n_S, m_c\right]\right\}\right|\right\} \tag{5}$$

with

$$\tilde{\chi}_{Q5}\left[n_S, m_c\right] \triangleq \tilde{\chi}_{Q5}\left(\tau_{n_S} - (\hat{\tau}_{n_S,0} + \frac{m_c d_c}{2f_c}), \Delta f\right)[n_S]$$

where m_c is the index of local code replica sequence related to code chip offsets; $\hat{m}_c$, $\hat{m}_u$, and $\hat{m}_p$ with the operator of $\hat{(\cdot)}$ denote the respective estimates based on the decision-making process above of their arguments; $DF^p\{\cdot\}$ is the digital operator of FRFT for an FRFT order p; $\hat{\tau}_{n_S,0}$ is the initial guess of the code phase delay, and it can be rewritten as $\hat{\tau}_{n_S,0} \triangleq \hat{\tau}_{n_C,N_S-1}$ if the S-LCI processing index is contained; τ_{n_S} represents the actual absolute code delay at the beginning of the n_Sth processing interval; f_c is the code rate; $\tilde{\chi}_{Q5}\left[n_S, m_c\right]$ is the measured noisy baseband CAF signal.

Then, the closed-form models of the matched frequency shift error and rate based on the digital FRFT are given by

$$\Delta f_{n_C}\left[\hat{m}'_u, \hat{m}_p\right] = \frac{\hat{m}'_u}{N_S T_S \sin\left(\alpha\left[\hat{m}_p\right]\right)} \tag{6}$$

$$\mu_{n_C}\left[\hat{m}_p\right] = -\frac{\cot\left(\alpha\left[\hat{m}_p\right]\right)}{N_S T_S^2} \tag{7}$$

where $\hat{m}'_u \triangleq \hat{m}_u/2/\sqrt{N_S}$; $\alpha\left[\hat{m}_p\right] = \frac{\pi}{2}\left(1 + \hat{m}_p \Delta p\right)$, and it is the matched rotation angle; the subscript n_C denotes the epoch index for the S-LCI correlations of the FRFD.

$$\tilde{\chi}_b^+\left[m_c,m_u,m_p\right]=\frac{\sqrt{1-j\cot\left(\alpha\left[m_p\right]\right)}}{2\sqrt{N_S}}\sum_{n_S=-N_S}^{N_S}\tilde{\chi}_{Q5}\left[\frac{n_S}{2\sqrt{N_S}},m_c\right]e^{\left(j\pi\frac{\cot\alpha[m_p]m_u^2}{4N_S}-j\pi\frac{\csc\alpha[m_p]m_un_S}{2N_S}+j\pi\frac{\cot\alpha[m_p]n_S^2}{4N_S}\right)} \tag{4}$$

After that, a frequency discriminator is used to reduce the estimated frequency error and optimize the frequency error estimation further, and it is computed as [36]

$$\begin{aligned}&\Delta\hat{f}_{disc,n_C}\\&=\frac{\left(\Delta f_{n_C}\left[\hat{m}_u'-1,\hat{m}_p\right]P_l+\Delta f_{n_C}\left[\hat{m}_u',\hat{m}_p\right]P_n+\Delta f_{n_C}\left[\hat{m}_u'+1,\hat{m}_p\right]P_h\right)}{P_l+P_n+P_h}\end{aligned} \tag{8}$$

with

$$P_l=\left|\tilde{\chi}_b^+\left[\hat{m}_u'-1,\hat{m}_p\right]\right|^2,\ P_n=\left|\tilde{\chi}_b^+\left[\hat{m}_u',\hat{m}_p\right]\right|^2,\ P_h=\left|\tilde{\chi}_b^+\left[\hat{m}_u'+1,\hat{m}_p\right]\right|^2$$

Next, the matched code phase offset is modeled as

$$\Delta\hat{\tau}_{n_s}\left[\hat{m}_c\right]\triangleq\tau_{n_S}-\left(\hat{\tau}_{n_S,0}+\frac{\hat{m}_cd_c}{2f_c}\right) \tag{9}$$

Finally, the carrier phase is discriminated by

$$\begin{aligned}\Delta\hat{\phi}_{disc,n_C}&=\operatorname{atan2}\left[\frac{\Im\left(\tilde{\chi}_b^+\left[\hat{m}_c,\hat{m}_u,\hat{m}_p\right]\right)}{\Re\left(\tilde{\chi}_b^+\left[\hat{m}_c,\hat{m}_u,\hat{m}_p\right]\right)}\right]\\&-\angle\left[\sqrt{1-j\cot\left(\alpha\left[\hat{m}_p\right]\right)}e^{j\pi\frac{\Delta\hat{f}_{n_C}^2\left(\Delta\hat{f}_0,\hat{\mu}_0\right)\cot\left(\alpha\left[\hat{m}_p\right]\right)}{N_S}}\right]\end{aligned} \tag{10}$$

where $\Delta\hat{f}_0$ and $\hat{\mu}_0$ represent the initial frequency offset and Doppler rate estimates, respectively.

3) Computation of carrier and code NCO frequencies: The carrier NCO frequency is computed as

$$\hat{f}_{\phi,NCO,n_C}=f_I+\hat{f}_{n_C} \tag{11}$$

with

$$\begin{aligned}\hat{f}_{n_C}&=\hat{f}_{n_C-1}+\mu_{n_C}\left[\hat{m}_p\right]T_t\\&+\Delta f_{n_C}\left[\hat{m}_u',\hat{m}_p\right]+\Delta\hat{f}_{disc,n_C}+\Delta\hat{\phi}_{disc,n_C}\end{aligned} \tag{12}$$

where f_I is the IF, T_t is the S-LCI interval, $\hat{f}_{n_C}$ and $\hat{f}_{n_C-1}$ are the estimated Doppler frequency in the current and previous S-LCI epochs, respectively.

On the other hand, the code NCO frequency is solely assisted by the carrier NCO frequency to alleviate the multipath interference on the code phase estimates. So, the code NCO frequency is given by

$$\hat{f}_{\tau,NCO,n_C}=f_c+f_c\Delta\hat{\tau}_{n_C}-\frac{f_c}{f_r}\hat{f}_{n_C} \tag{13}$$

where $\Delta\hat{\tau}_{n_C}$ is the matched code delay offset in the previous epoch; f_r is the RF.

It is worth mentioning that the NCO frequencies in this work are estimated as the average values for the next S-LCI epoch.

B. Generation of the super-resolution measurements

This part investigates the method to build the SRM, i.e., the Doppler frequency and pseudo-range measurements, from the proposed U-SRR.

1) Doppler frequency : The Doppler frequency measurement in the proposed U-SRR is the average value over the current S-LCI interval. So, it is obtained from

$$\tilde{f}_{dop,n_C}=\hat{f}_{n_C}$$

Then, the matched Doppler rate can estimate the instantaneous Doppler in the FRFD and the current Doppler measurement value. Hence, the instantaneous Doppler at the beginning of the n_Cth epoch is computed by

$$\hat{f}_{dop,n_C,0}=\tilde{f}_{dop,n_C}-\frac{1}{2}\mu_{n_C-1}\left[\hat{m}_p\right]T_t$$

Finally, both the Doppler measurement and the instantaneous Doppler estimates have been obtained in this work.

2) Pseudorange: GNSS receivers compute the user's position and velocity with the pseudorange and Doppler frequency measurements.

At first, for $n_S=0,\cdots,N_S-1$, $n_S\in\mathbb{Z}$, the generation of pseudorange measurements is computed through

$$\tilde{\rho}_{n_S}^i=c\left(\hat{t}_{n_S}^i-\hat{\tau}_{rem,n_S}^i-\frac{\hat{f}_{\tau,NCO,n_C}^i}{f_c}n_ST_S\right) \tag{14}$$

where n_S is the index of the CAF samples (3) since the S-LCI epoch n_C+1; the superscript i is the satellite number; $\hat{\tau}_{rem,n_S}^i$ is the remained code delay in seconds at the previous epoch; $\hat{t}_{n_S}^i$ is the local time count for the TOA of satellite i with an oven-controlled crystal oscillator (OCXO) in this work.

The code NCO frequency value is unchangeable over the period between epoch n_C+1 and n_C+2; the same case happens to the carrier frequency as well.

C. Computation of the positioning and velocity solutions

The architecture of the U-SRR is investigated in this work. However, we mainly focus on the baseband processing design other than the navigator of the receiver. Nevertheless, for the completeness of the context, this part briefly discusses the navigation algorithms.

For example, the user's velocity will be calculated from the SR Doppler set $\left\{\tilde{f}_{dop,n_C}^1,\ldots,\tilde{f}_{dop,n_C}^L\right\}$ based on the standard least-square (LS) method where the superscript L denotes the used satellite number in navigation. While the weighted LS algorithm estimates the user's positioning solution from the SR pseudorange set $\left\{\tilde{\rho}_{n_S}^1,\ldots,\tilde{\rho}_{n_S}^L\right\}$ and it is a single-point positioning (SPP) approach. The two methods can refer to an open-source package program, RTKLIB [37].

IV. Computation of Doppler and TOA References

TOA and Doppler frequency references will evaluate the accuracies of code phase and frequency errors. In that case, this section will introduce how to compute the reference values of the TOA and Doppler with the true user's position and velocity.

A. Doppler reference computation

The Doppler reference model is given by

$$f_{dop,k}^{i} = \frac{f_r}{c}\begin{bmatrix} \mathbf{v}_k - \mathbf{v}_k^i \\ \left(\delta \dot{t}_k - \delta \dot{t}_k^i\right) c \end{bmatrix}^T \cdot \left[\mathbf{e}_k^i, 1\right] \tag{15}$$

with

$$\mathbf{e}_k^i = \left[-\frac{\left(x_k^i - x_k\right)}{r_k^i}, -\frac{\left(y_k^i - y_k\right)}{r_k^i}, -\frac{\left(z_k^i - z_k\right)}{r_k^i}\right]$$

$$r_k^i = \|\mathbf{p}_k - \mathbf{p}_k^i\|$$

$$\mathbf{p}_k \triangleq [x_k, y_k, z_k]^T,\ \mathbf{p}_k^i \triangleq \left[x_k^i, y_k^i, z_k^i\right]^T$$

where c is the speed of light and subscript k denotes the navigation computation epoch index; $(\cdot)$ and $\|\cdot\|$ denotes the operators of inner product and Euclidean distance computation, respectively; $\mathbf{v}_k$ and $\mathbf{p}_k$ are the user's true velocity and position in the Earth-centered, Earth-fixed (ECEF) coordinate frame; $\mathbf{v}_k^i$, $\mathbf{p}_k^i$ and $\delta \dot{t}_k^i$ are the satellite velocity, position and clock drift, respectively, computed from the broadcast ephemeris; $\mathbf{e}_k^i$ is the direction cosine vector reference; r_k^i is the geometry distance reference between the satellite i and the receiver's antenna; finally, $\delta \dot{t}_k$ is the user's clock drift reference, and it is fitted from the velocity results of the proposed U-SRR in a post-processing way which is modeled as

$$\delta \dot{t}_k = \frac{1}{N_{Nav}}\left(\sum_{j=0}^{N_{Nav}-1} \delta \hat{\dot{t}}_j\right) \tag{16}$$

where $\delta \dot{t}_k$ is assumed to be not varied with time variable in this work, so it satisfies $\delta \dot{t}_k \triangleq \delta \dot{t}$; N_{Nav} is the navigation solution number over the total processing time, respectively; $\delta \hat{\dot{t}}_j$ is the estimated instantaneous clock drift at each short-time processing epoch.

B. TOA reference computation

The TOA reference will be obtained based on the computed Doppler reference. At first, the pseudorange reference is modeled as

$$\rho_k^i = r_k^i + c\delta t_k + A_k^i \tag{17}$$

where A_k^i is the atmospheric delay error reference which is obtained from the broadcast ephemeris where the ionospheric error computes from the Klobuchar model and the tropospheric one is from the Saastamoninen model; δt_k is the clock bias reference in seconds, and it is fitted from the positioning results of the proposed U-SRR and the clock drift reference. So, it is expressed as

$$c\delta t_k = c\delta \hat{t}_0 + c\delta \dot{t} k\Delta t \tag{18}$$

where $c\delta \hat{t}_0$ is the initially estimated clock bias from the proposed U-SRR; Δt is the processing interval between two adjacent navigation solutions. We use a high-quality OCXO embedded in the Labsat 3 Wideband to collect GPS IF data, so it is reasonable to fit the clock bias with a linear model. It is also worthwhile to mention that the geometry distance reference is a function of the local clock, that is

$$r_k^i \triangleq r_k^i\left(\hat{t}_k\right) \triangleq \|\mathbf{p}_k - \mathbf{p}_k^i\left(\hat{t}_k\right)\|$$

where $\hat{t}_k$ is the local clock time, $\mathbf{p}_k$ represents the true user's position here.

At last, the reference, which represents the truth TOA about satellite i in seconds, is obtained from

$$TOA_k^i = \frac{\left(\rho_k^i - c\delta t_k\right)}{c} \tag{19}$$

V. Removal of initial code phase errors

As discussed earlier, the proposed unassisted SRP fundamentally leverages a code phase DR manner based on the SR average Doppler frequency rate and instantaneous Doppler frequency shift. In other words, the initial or absolute code phase (corresponding to the initial positioning solution) at the start-off of the DR processing requires an initialization procedure like all the other DR sensors.

The specific objective of the code phase initialization is to determine a desirable initial code phase that accurately reflects the behavior of the LOS signal. It is imperative to underscore that this type of research focus pertains to an extensive domain of knowledge within the realm of the research interests, including but not limited to the advanced code discriminating methods [4]–[6] or ray tracing based 3D city model [14], [38]–[40]. Any further discussions related to this topic are beyond the scope of this study. Henceforth, the implementation details for the proposed code phase DR initialization will not be expounded anymore.

Notwithstanding, the initial code phase bias must be addressed for a sufficiently intuitive validation of the proposed algorithm. So, for the completeness of the context, we will have a quick introduction of the hardware-in-the-loop simulation to remove the initial biased error with the true position.

The original absolute code phase, which is assumed to be biased due to the NLOS/multipath interference in challenging environments, is given by $\hat{\tau}_{rem,0}^i$ earlier. Then, we have an accurate pseudorange prediction ρ_0^i simulated through the true position coordinates, the Klobuchar model, and the Saastamoninen model, as computed by (17). So, the code delay error in seconds can be modeled as

$$\Delta\tau_0^i = c^{-1}\left(\widetilde{\rho}_0^i - \rho_0^i\right)$$

where $\widetilde{\rho}_0^i$ is the measured pseudorange based on the proposed algorithm by (14), that is, $\widetilde{\rho}_0^i \triangleq \widetilde{\rho}_0^i\left(\hat{\tau}_{rem,0}^i\right)$; $\widetilde{\rho}_0^i(\cdot)$ can be defined as a function of its argument, namely $\hat{\tau}_{rem,0}^i$; the subscript 0 corresponds to the local receiver time with respect to the first IF sampling point at the first S-LCI interval leveraging the proposed algorithm. So, the updated absolute code phase by the true-position-based model is computed as

$$\hat{\tau}_{rem,n_S}^{i+} = \hat{\tau}_{rem,n_S}^i + \Delta\tau_0^i \tag{20}$$

Finally, the updated pseudorange measurement by the true-position-based model, i.e., the APA method, is given by

$$\widetilde{\rho}_{n_S}^{i+} = c\left(\hat{t}_{n_S}^i - \hat{\tau}_{rem,n_S}^{i+} - \frac{\hat{f}_{\tau,NCO,n_C}^i}{f_c} n_S T_S\right)$$

Therefore, $\widetilde{\rho}_{n_S}^{i+}$ is the updated pseudorange with the initial/absolute code phase removed. The SR positioning results based on the proposed U-SRR are assessed for comparative analysis and validation with the updated pseudorange subsequently.

In addition, the authors' recent publications provide a comprehensive exploration, evaluation, and discussion on this subject, focusing on a more meticulous methodology for aiding the tracking process of an on-the-fly GNSS receiver with the user's absolute position [25], [26].

VI. Real-world experiments and discussions

The GPS L5 IF data synchronized with a high-quality OCXO are collected with the LabSat 3 Wideband in a static open-sky and a dense-urban area. It is known that the GPS constellation consists of the medium Earth orbit (MEO) satellites, and the orbital period is approximately 12 hours. Therefore, we collected the data for two days at an identical time to guarantee the same geometry distribution of the constellation in the sky in the two testing situations. The IF sampling rate is 58 MHz with complex 2-bit quantization in the used frontend. A u-blox F9P device receives the GPS signals from the same antenna as the frontend used. The real-world environment view and the skyplots for the static test are illustrated in Fig. 4. The position of the user's antenna manually selected and confirmed in the Google Map determines the ground truth in the dense-urban experimental area, while the open-sky benchmark is from the mean value of the u-blox F9P solutions.

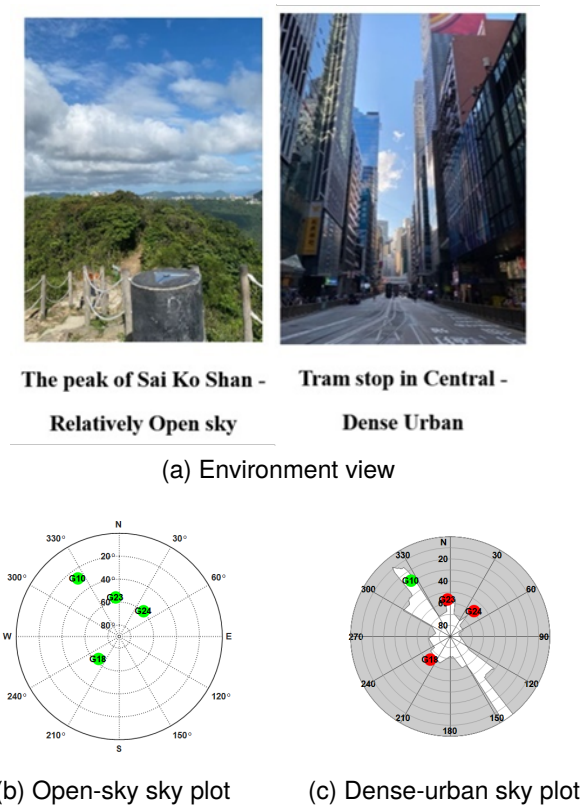

Fig. 4. Static experimental environments and sky plots.

A. S-LCI correlation power

The traditional correlating process typically leverages the subspace of frequency shift to estimate the unknown incoming signal. The estimating processing is based on the old fast Fourier transform (FFT) [14], [18], [19]. In contrast, the digital FRFT [34] used in the proposed SDR simultaneously matches the frequency shift and rate such that more abundant subspace related to the incoming signal features elevates the correlation estimation. The experimental results will verify this viewpoint.

The curves of correlation power in terms of the code error and Doppler rate offset are plotted as shown in Fig. 5, and the code error model satisfies

$$\delta\hat{\tau}_{n_C}^{(PRN)} \triangleq \Delta\hat{\tau}_{n_C,0}^{(PRN)}\left[\hat{m}_c\right] - \Delta\tau_{n_C}^{(PRN)} \tag{21}$$

where $\Delta\hat{\tau}_{n_C,0}\left[\hat{m}_c\right]$ is the matched code phase offset through (5) where the subscript $(n_C, 0)$ means the initial slow-time epoch over the n_Cth S-LCI interval; the superscript (PRN) denotes the PRN number; $\Delta\tau$ is its reference of which the model is

$$\Delta\tau_{n_C}^{(PRN)} \triangleq TOA_{n_C,0}^{(PRN)} + \delta t_{n_C,0} - \hat{\tau}_{n_C-1,N_S-1}^{(PRN)} \tag{22}$$

where $TOA_{n_C,0}$ and $\delta t_{n_C,0}$ are the respective TOA and clock bias error reference computed with (19) and (18), and $\hat{\tau}_{n_C-1,N_S-1}$ is the measured code phase delay at the beginning of the current processing interval.

As shown in Fig. 5, the S-LCI correlation power in the FRFD tested in the dense-urban area is larger than in the traditional FD. Besides, increasing the S-LCI interval improves the correlation power and reduces the code error simultaneously. Also, the longer the integration is, the higher the resolution of the Doppler rate estimation becomes.

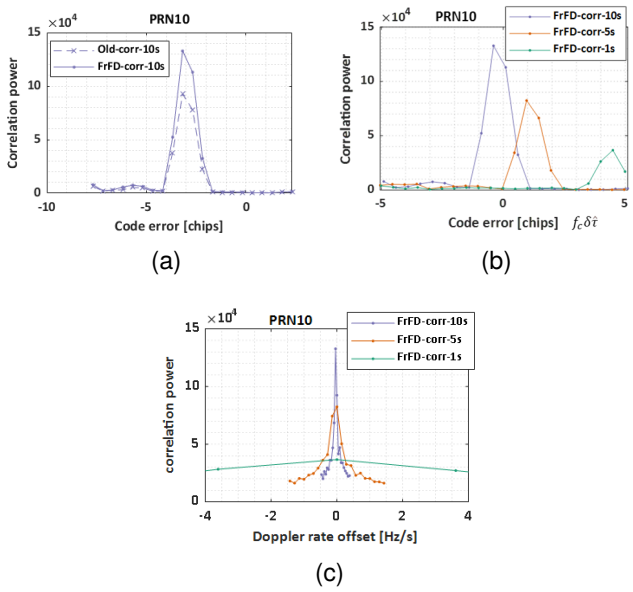

Fig. 5. Correlation power based on the proposed U-SRRs in the dense-urban area. The start processing GPS time is 207214.58 s. "Old-corr-10s" corresponds to a 10-s coherent integration process based on the old FFT.

The correlation power shape varying with the time in the open sky is plotted compared to the one in the dense-urban area, as shown in Fig. 6 and Fig. 7. The signals from the satellite SV23 and SV24 are taken to be an example where the U-SRR leverages

a 10-s S-LCI interval. The two cases prove that the proposed U-SRR algorithm still maintains the system reasonably estimating the signals even if irregular noise exists in the dense-urban area. For example, the correlation power does not fluctuate stably, and the signal strength varies radically. In contrast, it will be difficult for the traditional correlating process to reach this goal. After that, we will investigate how the SR correlation power in the dense-urban area affects the code phase and frequency errors produced by the traditional discriminator.

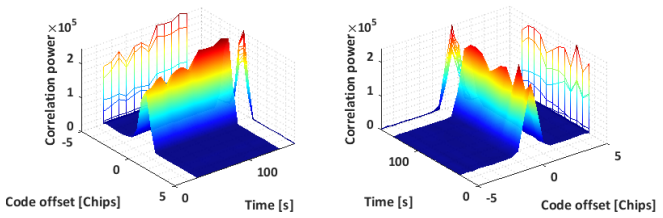

Fig. 6. Open-sky correlation power distribution about the code offset $\Delta\hat{\tau}_{n_S}$ $[\hat{m}_C]$ and the time variable from SV24 and SV23.

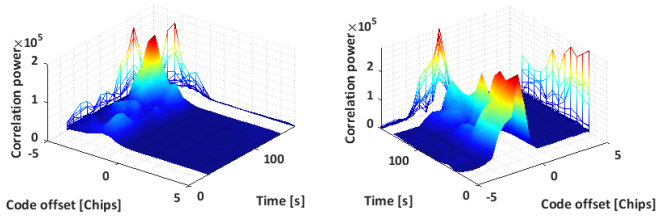

Fig. 7. Dense-urban correlation power distribution about the code offset $\Delta\hat{\tau}_{n_S}$ $[\hat{m}_C]$ and the time variable from SV24 and SV23.

The color maps of the SR correlation power are illustrated in Fig. 8. The results show that the traditional code phase estimates are close to the reference in the open-sky test. However, the estimated ones in the dense-urban case differ from the reference dramatically, even if the correlating process takes advantage of the S-LCI algorithm in this case.

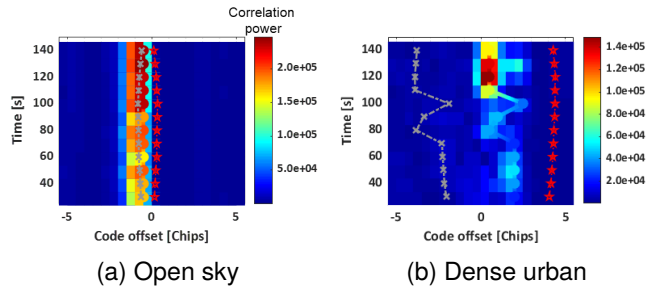

Fig. 8. 2D color maps of the SR correlation power w.r.t. code offset and time variables of SV24 from the open sky and dense-urban area, where the colorful, red, and grey markers correspond to the traditional code phase offset estimates (9), code phase offset reference (22) and their difference, respectively.

The CDF curves of the summed code errors from all the visible satellites are shown in Fig. 9. The urban environment causes much greater code errors than the open-sky ones in the traditional code discriminating process. In other words, the pseudorange measurement and positioning performances will fiercely drop if the code discriminator is not upgraded, even if the correlation makes use of the S-LCI approach. Under this circumstance, we consider using a SR Doppler frequency estimation to aid the code tracking to deal with this issue.

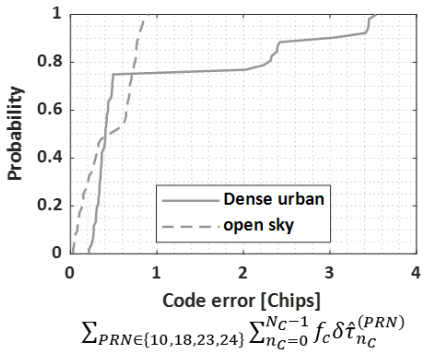

Fig. 9. CDF curves of the code errors summed from all the visible satellites based on the traditional code discriminating algorithm.

Therefore, we assess the SR correlation power of the frequency error. At first, the measured frequency offset is modeled as

$$\Delta\hat{f}_{n_C}^{(PRN)} \triangleq f_{n_C}^{(PRN)} - \hat{f}_{n_C}^{(PRN)} \tag{23}$$

where $\hat{f}_{n_C}$ refers to (12) and f_{n_C} denotes the true frequency measurement. Then, the frequency offset model is

$$\Delta f_{n_C}^{(PRN)} \triangleq f_{dop,n_C}^{(PRN)} + f_r\delta\dot{t} - \hat{f}_{n_C-1}^{(PRN)} \tag{24}$$

Finally, the Doppler frequency error is modeled as

$$\delta f_{n_C}^{(PRN)} \triangleq \Delta\hat{f}_{dop,n_C}^{(PRN)} - \Delta f_{dop,n_C}^{(PRN)} \tag{25}$$

where $\hat{f}_{n_C}^{(PRN)}$, $f_{dop,n_C}^{(PRN)}$, and $\delta\dot{t}$ are given by (12), (15), and (16), respectively. After that, it can be observed that the grey frequency error curves in Fig. 10 have different patterns from the ones of the code errors in Fig. 8. More specifically, in contrast to the code error curves, the Doppler frequency errors in the dense-urban area perform very close to the one in the open sky as their CDF curves, given in Fig. 11, are similar.

These experimental results prove that the proposed U-SRR elevates the Doppler estimation performance in a signal-difficult situation, even as accurately as of the one in the open sky. Therefore, it is convincing to aid the code phase estimation with the SR Doppler frequency.

Applying the SR Doppler to aid the code phase increases the precision of the pseudorange measurements. However, this method does not remove the initial bias of the code phase. In other words, the U-SRR cannot estimate the absolute position correctly once such an initial bias error exists. It is worth noting that the proposed U-SRR does not contribute to the correction of the initial bias, and we manually eliminate the bias with the APA method in the code tracking loop using a true position as introduced in Section V.

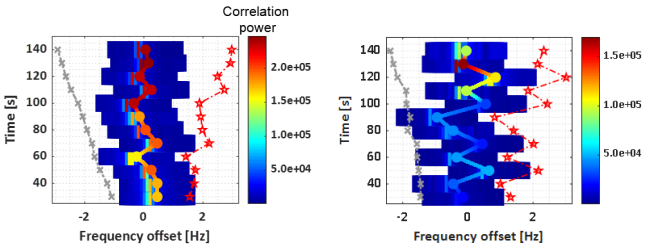

Fig. 10. Color maps of the SR correlation power w.r.t. frequency offset and time variables of SV24 from the open sky and dense-urban area where the colorful, red, and grey markers correspond to the traditional frequency offset estimates (23), frequency offset reference (24) and their difference, respectively.

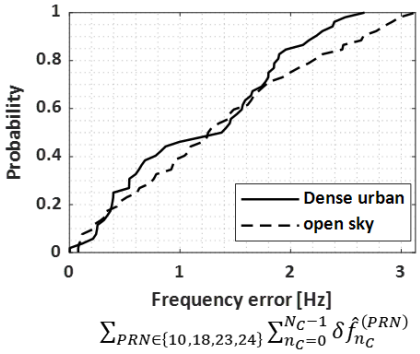

Fig. 11. CDF curves of the frequency errors summed from all the visible satellites.

Finally, how the 3D SR correlation power in the code domain varies with the time is displayed in Fig. 12, where the 2D correlation projections about the code offset and time are also illustrated. Again, the SR correlation distribution in the dense-urban area performs much more erratic and erroneous than in the open sky.

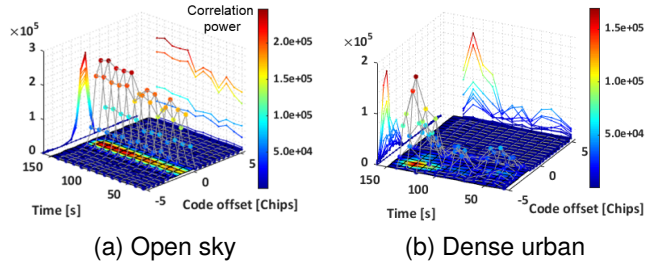

Fig. 12. 3D SR correlation power of SV24 in the code domain varying with the time in the open sky and dense-urban area.

Then, the projected code-time 2D power maps from the 3D SR correlation are given in Fig. 13. As verified, the proposed U-SRR baseband successfully achieves code phase estimation free from fluctuating SR correlation by utilizing SR Doppler aiding. On the other hand, the code estimates are further improved to be as accurate as those in the open sky under the condition of removing the initial code bias.

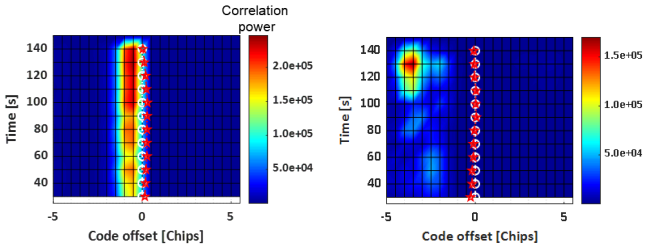

Fig. 13. Shading code-time 2D power map of SV24 projected from the 3D SR correlation in the open sky and dense-urban area. The white markers correspond to the measured code offset by the proposed U-SRR, i.e., $\Delta\hat{\tau}_{n_S}[\hat{m}_c] \equiv 0$, while the red markers represent the reference of the code offset (22).

Finally, we assess the CDF curves of the summed code errors from the proposed 10-s U-SRR after the initial bias error is removed. Moreover, it is also compared with the traditional code discriminating algorithm. The comparative results are plotted in Fig. 14. As observed, the proposed algorithm has vastly decreased the code error and significantly raised the estimation stability.

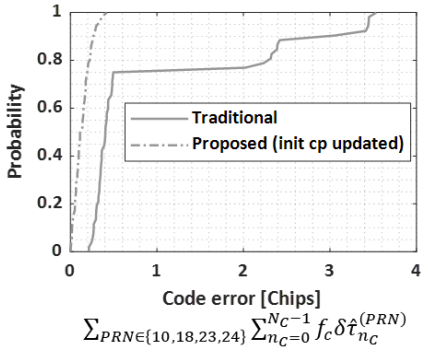

Fig. 14. CDF curves of the summed code errors in the dense-urban area. "init cp updated" corresponds to the removal of the initial code bias as introduced in Section V.

B. SR Doppler in the FRFD

In the proposed U-SRR, the Doppler rate of the incoming signals can be estimated with the FRFT, and this point is different from the current commercial GNSS receiver. Thus, in this part, the traditional NCO frequency and the one compensated by the Doppler rate estimation, i.e., the proposed NCO frequency, will be compared to show the superiority of the Doppler estimating process straightforwardly.

As provided in Fig. 15, if it does not compensate for the frequency change (i.e., the Doppler rate) over one coherent processing time, there is an explicit jump at the crossover of two adjacent S-LCI intervals. The problem can be solved by transferring the baseband signal (3) to the FRFD through (4). Finally, the proposed Doppler frequency in the FRFD becomes more continuous and accurate.

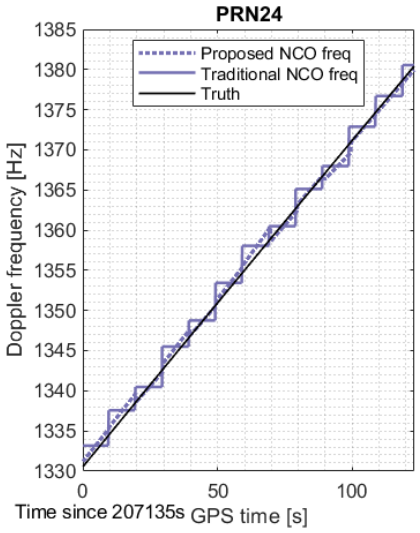

Fig. 15. Doppler estimation curves in the dense-urban area (Note: the time-domain NCO frequency curve of the proposed 10-s U-SRR here represents a mapping of its transformation in the FRFD and its real form in the time domain (before the digital FRFT) is identical to the curve of "Traditional NCO freq").

C. SR Doppler and TOA errors

In this section, we investigate the SR TOA and Doppler estimation accuracy compared to the reference predicted from the true position and velocity as computed from (19) and (15).

At first, we evaluate the estimates from SV24, which embraces the worst signal condition among the four available satellites in the dense-urban area. As for the traditional algorithms, Fig. 16 and Fig. 17 demonstrates that the L5Q signal processing with 20-ms coherent integration performs the best on the Doppler and TOA accuracy, while the 1-ms L1C/A signal case is the most robust as it lasts for the most extended stable tracking. However, all these tested old SDRs cannot work for the whole experiment time in the SV24 channel due to the violent signal variation.

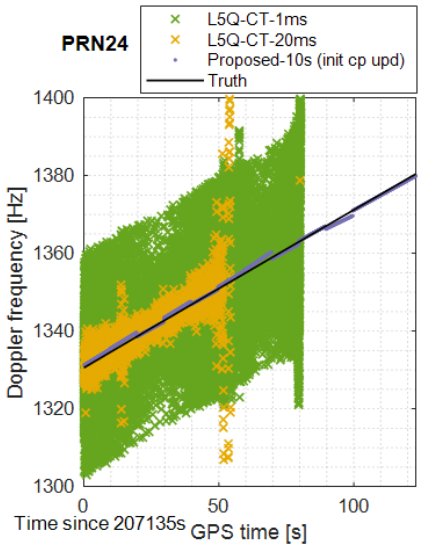

Fig. 16. Doppler estimation curves of SV24 based on different SDR algorithms in the dense-urban area. "init cp updated" corresponds to the removal of the initial code bias as introduced in Section V.

In contrast, the proposed U-SRR maintains excellent performances in accuracy and continuity in terms of both Doppler and TOA results. Moreover, Fig. 17 ((b) and (c)) shows that the 10-s U-SRR particularly has superior stability and anti-multipath ability than the 1-s and 5-s cases.

To sum up, the proposed 10-s U-SRR has 100% measurement availability versus the 20-ms traditional SDR of only 44.7%.

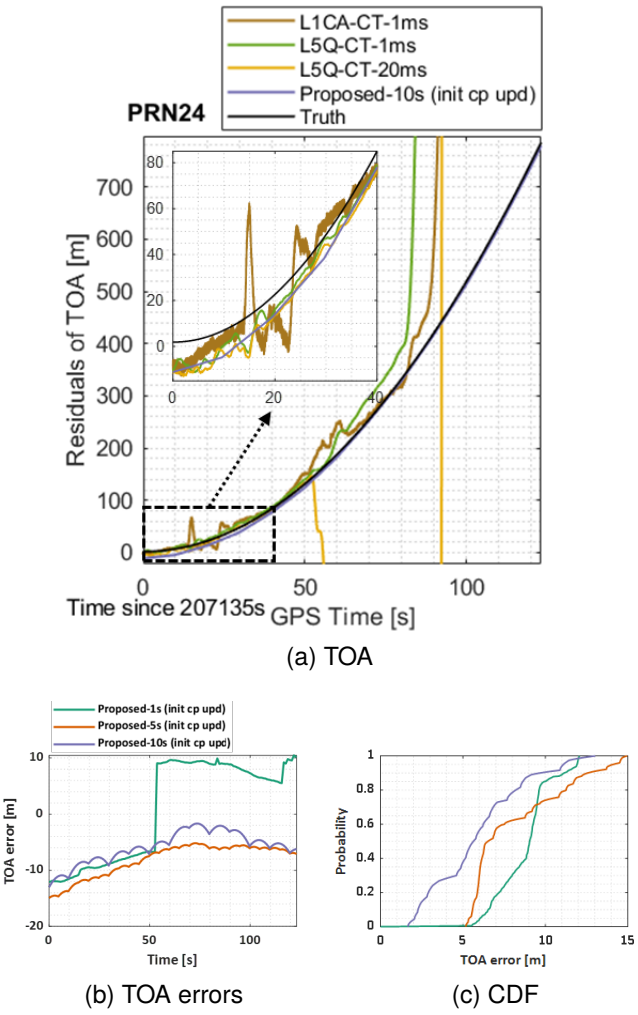

Fig. 17. TOA estimations, errors, and the corresponding CDF curves of SV24 based on different SDR algorithms in the dense-urban area. "init cp updated" corresponds to the removal of the initial code bias as introduced in Section V.

Next, the two medium-difficult cases of SV23 and SV18 in this dense-urban situation are also studied, and their TOA errors are illustrated in Fig. 18 and Fig. 19. As shown in Fig. 4, the sky mask indicates that the GNSS antenna received NLOS signals from these two satellites. According to the resultant curves, the proposed U-SRR produces less biased TOA and maintains more stable TOA estimates than the standard SDR outputs. Finally, the maximum TOA error within a 95% density has reduced by 31.6% and 28.5% for SV23 and SV18, respectively.

Finally, the least challenging case about the LOS satellite SV10 is assessed where the experiment copes with the Doppler estimation error. Thus, the curves of the Doppler error estimates are provided in Fig. 20. The proposed U-SRR estimates much less noisy Doppler measurements than the traditional SDR.

Likewise, the maximum frequency error within a 95% density has been decreased by 61.9%.

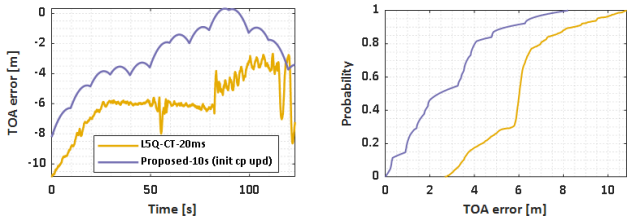

(a) TOA errors (b) CDF

Fig. 18. Curves of the TOA errors and the corresponding CDF of SV23 in the dense-urban area. "init cp updated" corresponds to the removal of the initial code bias as introduced in Section V.

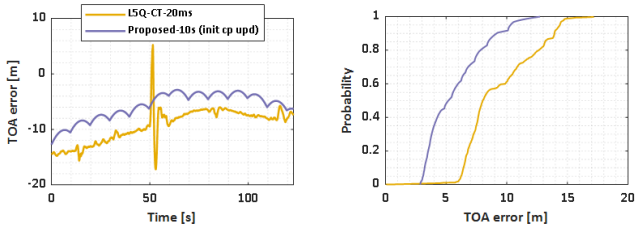

(a) TOA errors (b) CDF

Fig. 19. Curves of the TOA errors and the corresponding CDF of SV18 in the dense-urban area. "init cp updated" corresponds to the removal of the initial code bias as introduced in Section V.

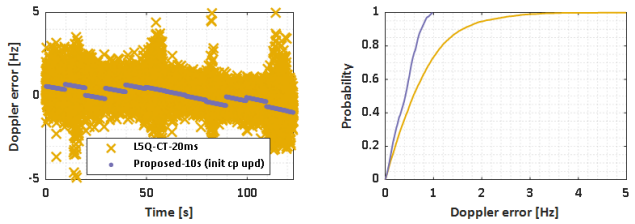

(a) Doppler errors (b) CDF

Fig. 20. Curves of the Doppler errors and the corresponding CDF of SV10 in the dense-urban area. "init cp updated" corresponds to the removal of the initial code bias as introduced in Section V.

D. SRP results

According to (15) and (19) to (25), the fitted clock bias and drift are inevitable to compute the code delay and Doppler frequency errors. Thus, we assess the clock drift and bias estimates at the first stage of the experiment.

In the beginning, the positioning errors from different SDRs are compared in Fig. 21. The traditional CT SDRs suffer severely in the dense-urban area, and none of them work over the entire testing time. Then, as expected, the positioning results from the proposed U-SRR and the positioning solutions (computed by the SPP engine of the RTKLIB package program) from the L1 C/A pseudoranges of the commercial u-blox F9P receiver (from the identical satellites) can continuously provide navigational results. However, the performance of the two results differs much. The positioning precision (the standard deviation of the estimates) of the proposed U-SRR is much higher than the F9P/RTKLIB-based results, while the latter is less biased than the former. The experimental results are reasonable as this work focuses on improving the Doppler accuracy (i.e., the positioning precision) other than removing the initial code bias error.

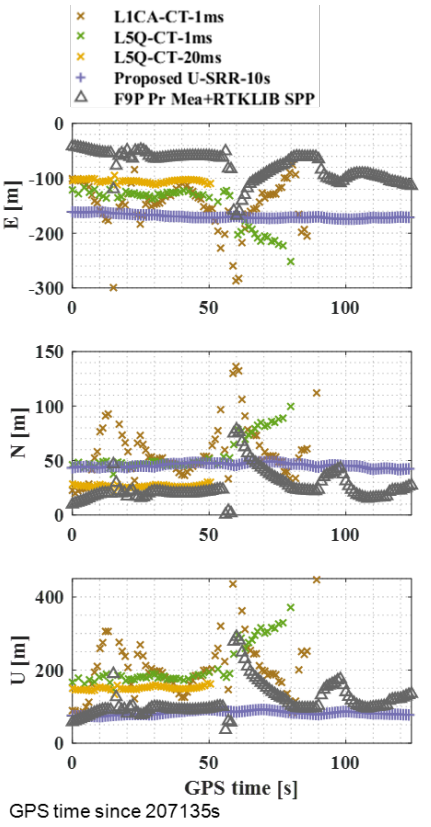

(a) Positioning errors

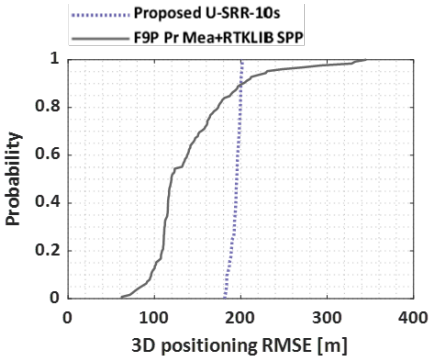

(b) CDF

Fig. 21. Comparison of the positioning errors and the corresponding CDF curves among traditional receivers and the proposed U-SRR. "F9P Pr Mea+RTKLIB SPP" corresponds to the single point positioning from the RTKLIB package based on the L1 C/A pseudoranges (from the identical satellites as used in the proposed U-SRR) produced by F9P.

Next, the initial code bias in the proposed U-SRR need to be eliminated to make the comparative analysis of the positioning estimation reasonably, where how to remove the initial code phase bias has been given by (20). Thus, the positioning accuracy (RMSE between the estimates and the truth) based on

the proposed U-SRR excluding the initial bias can be compared with the commercial receiver in this situation.

In the dense-urban area, Fig. 22 shows the proposed U-SRRs after the true position updates the initial code bias. Obviously, the proposed U-SRRs improve the positioning as the S-LCI interval increases. Therefore, the proposed navigation system explicitly shows tremendous potential in providing robust, constant, and high-accuracy navigation solutions in a highly challenging environment.

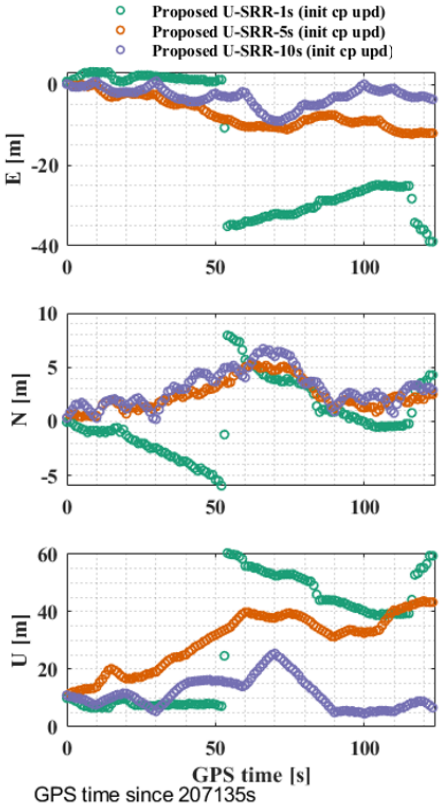

(a) Positioning errors

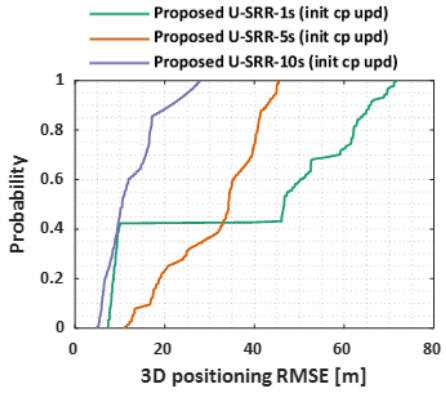

(b) CDF

Fig. 22. Comparison of the positioning errors and the corresponding CDF curves among traditional receivers and the proposed U-SRR with the initial bias removal algorithm. "init cp updated" corresponds to the removal of the initial code bias as introduced in Section V.

Therefore, Table II lists the positioning precision improvements in terms of different SDRs where "init cp updated" corresponds to the removal of the initial code bias as introduced in Section V. For example, increasing the S-LCI interval for the proposed U-SRR gives higher positioning precision. Also, it proves that the present initial code bias does not reduce its positioning precision.

TABLE II
POSITIONING PRECISION (STANDARD DEVIATION OF THE ESTIMATES) RESULTS AND IMPROVEMENTS.

Receivers	E [m]	N [m]	U [m]	3D [m]	Improvement
U-SRR-10s (init cp upd)	2.35	1.66	5.41	5.86	85.9%
U-SRR-5s (init cp upd)	3.79	1.38	9.58	10.17	75.6%
U-SRR-1s (init cp upd)	16.20	3.24	20.80	24.87	40.3%
U-SRR-10s	3.76	2.02	5.44	5.51	86.8%
F9P (L1CA+RTKLIB SPP)	22.97	10.46	33.35	41.69	-

As the proposed U-SRR using the 10-s S-LCI interval performs best among the tested GPS L5 SDRs, the fitted clock drift and bias are computed based on the 10-s S-LCI-based SRP solutions. Fig. 23 illustrates the fitted clock bias curve, which is also used for the previous S-LCI correlation power, SR Doppler and TOA error assessments.

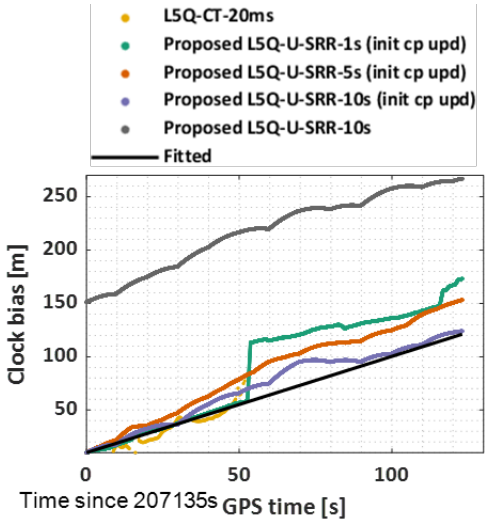

Fig. 23. Estimated clock biases from different U-SRRs and the fitted one from the 10-s U-SRR. "init cp updated" corresponds to the removal of the initial code bias as introduced in Section V.

One will also be very interested in the positioning discrepancy between the proposed U-SRR and a mature commercial receiver, e.g., the u-blox F9P. Hence, the positioning solutions of the proposed U-SRR with the initial code phase update are shown in the real-world map view in Fig. 24, where the commercial F9P real-time kinematic (RTK) solutions are also provided as intuitive proof of the extraordinary positioning performance of the proposed U-SRR towards the tested challenging environments. It must underscore that the F9P receiver cannot output fixed positioning solutions in this severely contested situation.

Under this circumstance, the proposed 10-s U-SRR using the SPP exhibits a very close positioning performance as the F9P. It is also worth mentioning that such advanced results are solely achieved with four satellites, three of which are NLOS. The proposed SRP accuracy can be further elevated when more

satellites, more types of GNSS measurements, more optimized signal processing, and advanced positioning and navigation algorithms are used, which will be completed in our future work.

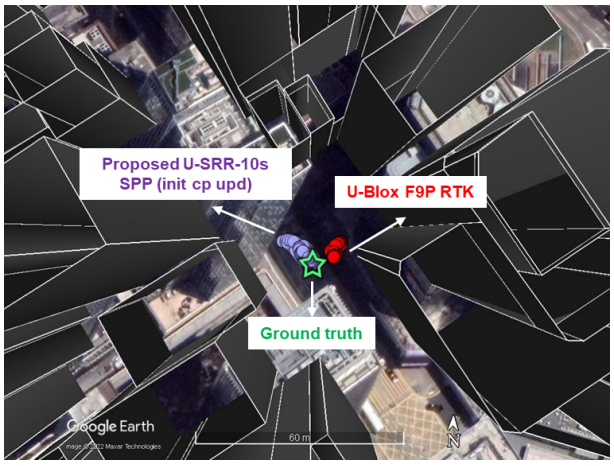

Fig. 24. Positioning results in the dense-urban area with the proposed U-SRR SPP and the u-blox F9P RTK (only float solutions can be available) displayed in the Google Map. "init cp updated" corresponds to the removal of the initial code bias as introduced in Section V.

VII. Conclusions

We proposed an unassisted super-resolution (SR) software-defined radio (SDR) using the GPS L5 signals in this work. First, the SR average Doppler rate and instantaneous Doppler frequency are estimated using the S-LCI correlations in the fractional Fourier domain (FRFD). Then, a code phase dead reckoning (DR) method is proposed to enhance the discriminating process of code tracking for multipath mitigation. Next, the L5I channel provides the ephemeris, and the SR pseudoranges from the L5Q channel are used to compute the high-accuracy user's positioning independently. The proposed unassisted SR receiver (U-SRR) has been experimented and validated in the real-world dense-urban area, and it has shown excellent performances as follows:

1) In comparison with the traditional 20-ms coherent tracking, the availability of the measurement from the NLOS satellite has been increased from 44.7% to 100%;
2) Both maximum TOA and Doppler frequency errors have been efficiently reduced compared to the traditional tracking algorithms, and the SPP precision has risen by 86.8% when it is compared with the L1 C/A pseudorange measurements produced by the commercial F9P receiver;
3) The single-frequency/constellation SPP based on the proposed U-SRR on the condition that the initial code bias is removed achieved a similar positioning accuracy to the u-blox F9P RTK results in the tested extremely dense-urban canyon.

Lastly, we must indicate the limitations this work undertakes, that a very high-quality clock, OCXO, is employed in this paper. Therefore, the clock error instability will cause a notable concern in the practical application. Besides, in its current form, the proposed architecture cannot adapt to kinematic navigation. In addition, the accurate initial/absolute code phase estimation should be addressed to enable its on-the-fly application. These issues will be worked on in the future.

Acknowledgment

This research has been supported by the funding of Prof. Naser El-Sheimy from NSERC CREATE and Canada Research Chairs programs.

References

[1] X. Chen, F. Dovis, S. Peng, and Y. Morton, "Comparative studies of gps multipath mitigation methods performance," *IEEE Transactions on Aerospace and Electronic Systems*, vol. 49, no. 3, pp. 1555–1568, 2013.
[2] P. Xie and M. G. Petovello, "Measuring gnss multipath distributions in urban canyon environments," *IEEE Transactions on Instrumentation and Measurement*, vol. 64, no. 2, pp. 366–377, 2014.
[3] T. Pany and B. Eissfeller, "Use of a Vector Delay Lock Loop Receiver for GNSS Signal Power Analysis in Bad Signal Conditions," in *2006 IEEE/ION Position, Location, And Navigation Symposium*, vol. 2006. IEEE, 2006, pp. 893–903.
[4] V. A. Veitsel, A. V. Zhdanov, and M. I. Zhodzishsky, "The mitigation of multipath errors by strobe correlators in gps/glonass receivers," *GPS Solutions*, vol. 2, no. 2, pp. 38–45, 1998.
[5] G. A. McGraw and M. S. Braasch, "Gnss multipath mitigation using gated and high resolution correlator concepts," in *Proceedings of the 1999 national technical meeting of the institute of navigation*, 1999, pp. 333–342.
[6] R. D. Van Nee, J. Siereveld, P. C. Fenton, and B. R. Townsend, "The multipath estimating delay lock loop: approaching theoretical accuracy limits," in *Proceedings of 1994 IEEE Position, Location and Navigation Symposium-PLANS'94*. IEEE, 1994, pp. 246–251.
[7] L. R. Weill, "Multipath mitigation using modernized gps signals: how good can it get?" in *Proceedings of the 15th International Technical Meeting of the Satellite Division of The Institute of Navigation (ION GPS 2002)*, 2002, pp. 493–505.
[8] P. C. Fenton and J. Jones, "The theory and performance of novatel inc.'s vision correlator," in *Proceedings of the 18th International Technical Meeting of the Satellite Division of The Institute of Navigation (ION GNSS 2005)*, 2005, pp. 2178–2186.
[9] S. Daneshmand and G. Lachapelle, "Integration of gnss and ins with a phased array antenna," *Gps Solutions*, vol. 22, no. 1, pp. 1–14, 2018.
[10] E. A. Marranghelli, R. L. La Valle, and P. A. Roncagliolo, "Simple and effective gnss spatial processing using a low-cost compact antenna array," *IEEE Transactions on Aerospace and Electronic Systems*, vol. 57, no. 5, pp. 3479–3491, 2021.
[11] X. Hong, W. Wang, N. Chang, and Q. Yin, "A subspace-based code tracking loop design for gps multi-antenna receiver in multipath environment," *GPS Solutions*, vol. 24, no. 4, pp. 1–17, 2020.
[12] N. I. Ziedan, "Optimized position estimation in mobile multipath environments using machine learning," *NAVIGATION: Journal of the Institute of Navigation*, vol. 70, p. navi.569, 3 2023. [Online]. Available: http://navi.ion.org/lookup/doi/10.33012/navi.569
[13] D. Borio, C. O'Driscoll, and G. Lachapelle, "Coherent, noncoherent, and differentially coherent combining techniques for acquisition of new composite gnss signals," *IEEE Transactions on Aerospace and Electronic Systems*, vol. 45, no. 3, pp. 1227–1240, 2009.
[14] N. S. Gowdayyanadoddi, J. T. Curran, A. Broumandan, and G. Lachapelle, "A Ray-Tracing Technique to Characterize GPS Multipath in the Frequency Domain," *International Journal of Navigation and Observation*, vol. 2015, pp. 1–16, sep 2015.
[15] N. S. Gowdayyanadoddi, A. Broumandan, J. T. Curran, and G. Lachapelle, "Benefits of an ultra stable oscillator for long coherent integration," in *Proceedings of the 27th International Technical Meeting of The Satellite Division of the Institute of Navigation (ION GNSS+ 2014)*, 2014, pp. 1578–1594.
[16] A. Soloviev and J. Dickman, "Extending GPS carrier phase availability indoors with a deeply integrated receiver architecture," *IEEE Wireless Communications*, vol. 18, no. 2, pp. 36–44, apr 2011. [Online]. Available: http://ieeexplore.ieee.org/document/5751294/
[17] R. Faragher, M. Powe, P. Esteves, N. Couronneau, M. Crockett, H. Martin, E. Ziglioli, and C. Higgins, "Supercorrelation as a Service: S-GNSS Upgrades for Smartdevices," in *Proceedings of the 32nd International Technical Meeting of the Satellite Division of The Institute of Navigation (ION GNSS+ 2019), September 16 - 20*, Miami, Florida, USA, 2019.

[18] P. D. Groves, Q. Zhong, R. Faragher, and P. Esteves, "Combining Inertially-aided Extended Coherent Integration (Supercorrelation) with 3D-Mapping-Aided GNSS," in *Proceedings of the 33rd International Technical Meeting of the Satellite Division of The Institute of Navigation (ION GNSS+ 2020), September*, 2020, pp. 2327 – 2346.

[19] C. Yang, A. Soloviev, A. Vadlamani, and J. C. Ha, "Coherent combining and long coherent integration for boc signal acquisition under strong interference," *NAVIGATION: Journal of the Institute of Navigation*, vol. 69, no. 1, 2022.

[20] T. E. Humphreys, M. J. Murrian, and L. Narula, "Deep-Urban Unaided Precise Global Navigation Satellite System Vehicle Positioning," *IEEE Intelligent Transportation Systems Magazine*, vol. 12, no. 3, pp. 109–122, 2020.

[21] Y. Luo, L.-T. Hsu, and Y. Pan, "A super-resolution algorithm with frft towards gnss toa estimation for multipath channel," in *Proceedings of the 34th International Technical Meeting of the Satellite Division of The Institute of Navigation (ION GNSS+ 2021)*, 2021, pp. 3350–3359.

[22] Y. Luo, L. Zhang, and H. Ruan, "An Acquisition Algorithm Based on FRFT for Weak GNSS Signals in A Dynamic Environment," *IEEE Communications Letters*, vol. 22, no. 6, pp. 1212–1215, jun 2018. [Online]. Available: https://ieeexplore.ieee.org/document/8344115/

[23] Y. Luo, C. Yu, S. Chen, J. Li, H. Ruan, and N. El-Sheimy, "A Novel Doppler Rate Estimator Based on Fractional Fourier Transform for High-Dynamic GNSS Signal," *IEEE Access*, vol. 7, pp. 29 575–29 596, 2019. [Online]. Available: https://ieeexplore.ieee.org/document/8660391/

[24] Y. Luo, H. Li-Ta, and N. El-Sheimy, "A Baseband MLE for Snapshot GNSS Receiver Using Super-Long-Coherent Correlation in a Fractional Fourier Domain," *unpublished*.

[25] Y. Luo, L.-T. Hsu, Z. Zhang, and N. El-Sheimy, "Improving gnss baseband using an rtk-position-aided code tracking algorithm," *GPS Solutions*, vol. 26, p. 125, 10 2022. [Online]. Available: https://link.springer.com/10.1007/s10291-022-01305-4

[26] Y. Luo, L.-T. Hsu, Y. Jiang, B. Liu, Z. Zhang, Y. Xiang, and N. El-Sheimy, "High-accuracy absolute-position-aided code phase tracking based on rtk/ins deep integration in challenging static scenarios," *Remote Sensing*, vol. 15, p. 1114, 2 2023. [Online]. Available: https://www.mdpi.com/2072-4292/15/4/1114

[27] Y. Luo, L. Zhang, and N. El-Sheimy, "An improved DE-KFL for BOC signal tracking assisted by FRFT in a highly dynamic environment," in *2018 IEEE/ION Position, Location and Navigation Symposium, PLANS 2018 - Proceedings*. IEEE, apr 2018, pp. 1525–1534.

[28] C. J. Hegarty, "Optimal and near-optimal detectors for acquisition of the gps l5 signal," in *Proceedings of the 2006 National Technical Meeting of The Institute of Navigation*, 2006, pp. 717–725.

[29] E. D. Kaplan and C. Hegarty, *Understanding GPS/GNSS. Principles and applications*, 3rd ed. Artech house, 2017.

[30] C. Hegarty, M. Tran, and A. Van Dierendonck, "Acquisition algorithms for the gps l5 signal," in *Proceedings of the 16th International Technical Meeting of the Satellite Division of the Institute of Navigation (ION GPS/GNSS 2003)*, 2003, pp. 165–177.

[31] Y. Luo, J. Li, C. Yu, Z. Lyu, Z. Yue, and N. El-Sheimy, "A GNSS Software-Defined Receiver with Vector Tracking Techniques for Land Vehicle Navigation," in *Proceedings of the ION 2019 Pacific PNT Meeting, Honolulu, Hawaii, USA*, 2019, pp. 713–727. [Online]. Available: https://www.ion.org/publications/abstract.cfm?articleID=16834

[32] A. J. V. Dierendonck, "GPS Receivers," in *Global Positioning System: Theory and Applications, Volume 1*, B. W. Parkinson, J. J. Spilker Jr, P. Axelrad, and P. Enge, Eds. Washington D.C.: American Institute of Aeronautics and Astronautics, Inc., 1996.

[33] "Navstar GPS Space Segment/ User Segment L5 Interfaces (IS-GPS-705H)." [Online]. Available: https://www.gps.gov/technical/icwg/IS-GPS-705H.pdf

[34] H. M. Ozaktas, O. Arikan, M. A. Kutay, and G. Bozdagt, "Digital computation of the fractional fourier transform," *IEEE Transactions on signal processing*, vol. 44, no. 9, pp. 2141–2150, 1996.

[35] H. M. Ozaktas and M. A. Kutay, "The Fractional Fourier Transform," in *European Control Conference (ECC), Porto, Portugal*, 2001, pp. 1477–1483.

[36] K. Yan, N. I. Ziedan, H. Zhang, W. Guo, X. Niu, and J. Liu, "Weak gps signal tracking using fft discriminator in open loop receiver," *GPS solutions*, vol. 20, no. 2, pp. 225–237, 2016.

[37] T. Takasu and A. Yasuda, "Development of the low-cost RTK-GPS receiver with an open source program package RTKLIB," in *Proceedings of the International symposium on GPS/GNSS, Jeju, Korea*, 2009, pp. 4–6.

[38] L. Lau and P. Cross, "Development and testing of a new ray-tracing approach to GNSS carrier-phase multipath modelling," *Journal of Geodesy*, vol. 81, no. 11, pp. 713–732, oct 2007.

[39] L.-T. Hsu, Y. Gu, and S. Kamijo, "3d building model-based pedestrian positioning method using gps/glonass/qzss and its reliability calculation," *GPS solutions*, vol. 20, no. 3, pp. 413–428, 2016.

[40] K. Strandjord, P. Axelrad, D. M. Akos, and S. Mohiuddin, "Improved Urban Navigation with Direct Positioning and Specular Matching," in *Proceedings of the 2020 International Technical Meeting of The Institute of Navigation, January 21 - 24*, 2020, pp. 787 – 800.

Yiran Luo is currently a postdoctoral associate at the University of Calgary. She received the joint Ph.D. degrees with the Department of Geomatics Engineering, University of Calgary, Canada, and with the School of Information and Electronics, Beijing Institute of Technology, China, respectively, in 2020. From 2020 to 2021, she was a Postdoctoral Fellow with the Department of Aeronautical and Aviation Engineering, Hong Kong Polytechnic University. Her research interests include GNSS signal processing, GNSS software-defined radio (SDR) design, and navigation and localization in harsh environments.

Li-Ta Hsu (S'09-M'15) received the B.S. and Ph.D. degrees in aeronautics and astronautics from National Cheng Kung University, Taiwan, in 2007 and 2013, respectively. He is currently an assistant professor with the Department of Aeronautical and Aviation Engineering, Hong Kong Polytechnic University, before he served as post-doctoral researcher in Institute of Industrial Science at University of Tokyo, Japan. In 2012, he was a visiting scholar in University College London, U.K. He is an Associate Fellow of RIN. His research interests include GNSS positioning in challenging environments and localisation for pedestrian, autonomous driving vehicle and unmanned aerial vehicle.

Chin-Lok Tsang is currently a final year undergraduate student majoring in aviation engineering and minoring in electronic and information engineering at the Hong Kong Polytechnic University. His research interests include GNSS signal processing, GNSS software-defined radio (SDR) design, and navigation and localization in harsh environments.

Naser El-Sheimy is currently a Professor at the Department of Geomatics Engineering, University of Calgary. He is the Tier-I Canada Research Chair in Geomatics Multi-Sensor Systems. He is a fellow of the Canadian Academy of Engineering and the U.S. Institute of Navigation. His research expertise includes geomatics multi-sensor systems, GPS/INS integration, and mobile mapping systems.